φ photoproduction with coupled-channel effects

Hui-Young Ryu[1,2], Alexander I. Titov[2,3], Atsushi Hosaka[3], and Hyun-Chul Kim[4,5,*]

[1]*Korea Institute of Science and Technology Information (KISTI) 245, Daejeon 305-806, Korea*
[2]*Research Center for Nuclear Physics, Osaka University, Ibaraki 567-0047, Japan*
[3]*Bogoliubov Laboratory of Theoretical Physics, JINR, Dubna 141980, Russia*
[4]*Department of Physics, Inha University, Incheon 402-751, Republic of Korea*
[5]*School of Physics, Korea Institute for Advanced Study, Seoul 130-722, Republic of Korea*
*E-mail: hchkim@inha.ac.kr

....
We study ϕ photoproduction with various hadronic rescattering contributions included, in addition to the Pomeron and pseudoscalar meson-exchange diagrams. We find that the hadronic rescattering diagrams can explain the recent experimental data in the vicinity of the threshold. In particular, the bump-like structure at the photon energy $E_\gamma \approx 2.3$ GeV is well explained by the $K\Lambda(1520)$ rescattering amplitude in the intermediate state, which is the dominant contribution among other hadronic contributions. We also find that the hadronic rescattering diagrams are consistent with the observed spin-density matrix elements near the threshold region.
....
Subject Index   D32

1. Introduction

The $\phi(1020)$ meson is distinguished from other vector mesons, since it contains mainly strange quarks. Because of its dominant strange quark content, its decays to lighter mesons and coupling to the nucleon are known to be suppressed by the Okubo–Zweig–Iizuka (OZI) rule. In fact, the strange vector form factors of the nucleon, which is implicitly related to the ϕ meson via vector meson dominance, is reported to be rather small [1]. This large $s\bar{s}$ content of the ϕ meson makes the meson exchange picture unfavorable in describing photoproduction of the ϕ meson. Thus, the Pomeron [2,3] is believed to be the main contribution to ϕ photoproduction, since it explains the slow rise of the differential cross sections of ϕ photoproduction as the energy increases. However, while it is true in the higher energy regime, a recent measurement reported by the LEPS collaboration [4] shows a bump-like structure around the photon energy $E_\gamma \approx 2.3$ GeV. It seems that the Pomeron alone cannot account for this bump-like structure, and that one should consider other production mechanisms of ϕ photoproduction near the threshold energy.

So far, the theoretical understanding of the production mechanism for ϕ photoproduction can be summarized as follows:

○ General energy dependence of the cross sections is mainly explained by Pomeron exchange that can be taken as either a scalar meson or a vector meson with charge conjugation $C = +1$. While the Pomeron explains the increase of the differential cross section $d\sigma/dt$ in the forward direction, it cannot describe the behavior of $d\sigma/dt$ near the threshold.

○ The exchange of neutral pseudoscalar mesons (π^0, η) provides a certain contribution to $d\sigma/dt$ near the threshold but it is not enough to explain the threshold behavior of $d\sigma/dt$ [5]. Moreover, π^0 and η exchanges taken alone, being their unnatural parity nature, wrongly predict the spin-density observables and, in particular, the ρ^1_{1-1} matrix element [6] (see Appendix A for its definition).

○ Usual vector meson exchanges such as ρ and ω are forbidden due to their negative charge conjugations ($C = -1$). Otherwise, the charge conjugation symmetry will be broken.

○ Vector meson exchanges with exotic quantum number such as $I(J^{PC}) = 1(1^{-+})$ are allowed, but these vector mesons, possibly hybrid exotic mesons, are not much known experimentally [7].

Understanding this present theoretical and experimental situation in ϕ photoproduction, Ozaki et al. [8] proposed a coupled-channel effect based on the K-matrix formalism. They considered the $\gamma N \rightarrow K\Lambda^*(1520)$ and $K\Lambda^* \rightarrow \phi N$ kernels [9] in the coupled-channel formalism in addition to $\gamma N \rightarrow \phi N$ and $\phi N \rightarrow \phi N$. It is a very plausible idea: since the threshold energy for the $K\Lambda^*$ is quite close to that for the bump-like structure ($E_\gamma \approx 2.3$ GeV), the $\Lambda^*(1520)$ resonance may influence ϕ photoproduction. Moreover, the $\gamma p \rightarrow K\Lambda^*(1520)$ reaction can be regarded as a subreaction for the $\gamma p \rightarrow K\overline{K}p$ process together with the $\gamma p \rightarrow \phi p$ one in Ref. [9]. In addition, a possible nucleon resonance ($J^P = 1/2^-$) with large $s\bar{s}$ content was also taken into account. Interestingly, the coupled-channel effects were shown to be not enough to explain the bump-like structure $E_\gamma \approx 2.3$ GeV. On the other hand, the bump-like structure was described by their possible N^* resonance and was interpreted as a destructive interference arising from the N^* resonance [10,11].

In the present work, we want to scrutinize in detail the nontrivial hadronic contributions arising from hadronic rescattering amplitudes in addition to Pomeron and pseudoscalar meson exchanges, by reexamining the previous work of Ref. [8]. We postulate that the Pomeron amplitude near the threshold region is suppressed, while the production mechanism there is explained by hadrons. We believe that such an attempt is legitimate because we do not know much about the Pomeron at low energies, while it is well established that it plays the dominant role at high energies. Thus we determine the threshold parameter in such a way that the Pomeron exchange becomes ineffective in the threshold energy region.

For hadronic processes, we take into account seven possible rescattering amplitudes with intermdiate ρN, ωN, σN, πN, $K\Lambda(1116)$, $K^*\Lambda(1116)$, and $K\Lambda(1520)$ states. However, it is quite involved to compute these rescattering equations explicitly, so we use the Landau–Cutkosky rule [12,13], which yields the imaginary part of the rescattering amplitudes by its discontinuity across the branch cut. Though their real part will surely contribute to the transition amplitude, we will show that the imaginary part already illuminates the coupled-channel effects on the production mechanism of $\gamma p \rightarrow \phi p$ near the threshold. The parameters such as the coupling constants and cut-off masses of the form factors will be fixed by describing the corresponding processes and by using experimental and empirical data. Yet unknown parameters are varied as compared to the present experimental data.

In the present work, we do not consider s-channel N^* resonances, since we do not have much information on them above the ϕN threshold [7]. Moreover, it is not necessary to introduce the N^* with large hidden strangeness, which was considered in Refs. [10,11] in an attempt to describe the LEPS data.

We will show that the hadronic mechanism with coupled-channel effects are indeed essential in explaining the recent LEPS data, which is a different conclusion from Ref. [8]. Therefore, we assert in this work that the main contribution in the vicinity of the threshold comes from

the hadronic coupled-channel effects, in particular, the $K\Lambda(1520)$ rescattering effects, while the Pomeron becomes important only at higher energies.

The present paper is organized as follows. In Sect. 2, we explain the basic formalism. We show how to compute the rescattering effects mentioned above. In Sect. 3, we present the numerical results such as the energy dependence of the forward cross sections, the angular distributions, and the spin observables. We also discuss how the $K\Lambda^*(1520)$ channel can explain the bump-like structure together with the tuned Pomeron exchange. We discuss in detail the spin-density matrix elements for ϕ photoproduction. The final section is devoted to summary and outlook. In Appendix A, we present the definition of the spin-density matrix elements for reference.

2.   General formalism

In the present work, we will employ the effective Lagrangian approach in addition to Pomeron exchange. In Fig. 1, we draw the relevant Feynman diagrams involved in describing ϕ photoproduction. The first diagram corresponds to the Pomeron exchange, and the second one depicts π^0 and η exchanges. The last diagram represents generically all the contributions from various rescattering amplitudes with intermediate hadron states, i.e. ρN, ωN, σN, πN, $K\Lambda(1116)$, $K^*\Lambda(1116)$, and $K\Lambda(1520)$, among which the last one was already considered in Ref. [8]. From now on, we will simply define the ρN rescattering amplitude as that with intermediate ρ and N states, and so on. We also define the four-momenta of the incoming photon, outgoing ϕ, the initial (target) proton, and the final (recoil) proton as k_1 and k_2, p_1 and p_2, respectively. In the center of mass (CM) frame, these variables are written as $k_1 = (k, \boldsymbol{k})$, $k_2 = (E_\phi, \boldsymbol{p})$, $p_1 = (E_p, -\boldsymbol{k})$, and $p_2 = (E_{p'}, -\boldsymbol{p})$, where $k = |\boldsymbol{k}|$, $E_\phi = \sqrt{m_\phi^2 + |\boldsymbol{p}|^2}$, $E_p = \sqrt{m_p^2 + |\boldsymbol{k}|^2}$, and $E_{p'} = \sqrt{m_{p'}^2 + |\boldsymbol{p}|^2}$, respectively.

The invariant amplitude related to the diagrams in Fig. 1 can be expressed as the Blankenbecler–Sugar (BbS) equation [14]

$$\mathcal{M}_{\gamma N \to \phi N}(p, p'; s) = \mathcal{M}^{\text{Born}}_{\gamma N \to \phi N}(p, p'; s) + \sum_i \int \mathrm{d}^3 q \, \frac{E_{M_i} + E_{B_i}}{(2\pi)^3 2 E_{M_i} E_{B_i}} \mathcal{M}_{\gamma N \to M_i B_i}(p, q; s)$$

$$\frac{1}{s^2 - (E_{M_i} + E_{B_i})^2 + i\varepsilon} \mathcal{M}_{M_i B_i \to \phi N}(q, p'; s), \tag{1}$$

which was derived from the three-dimensional reduction of the Bethe–Salpeter equation. The amplitude $\mathcal{M}^{\text{Born}}_{\gamma N \to \phi N}$ includes all the diagrams at the tree level. On the other hand, $\mathcal{M}_{\gamma N \to M_i B_i}(p, k; s)$ and $\mathcal{M}_{M_i B_i \to \phi N}(k, p'; s)$ are the off-mass-shell extended diagrams for the $\gamma p \to M_i B_i$ and
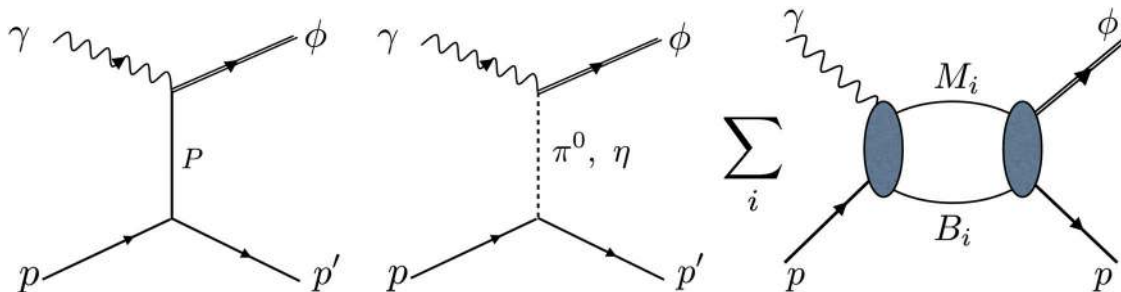

Fig. 1.   Relevant Feynman diagrams for ϕ photoproduction: We draw, from the left, the diffractive Pomeron exchange, the pseudoscalar meson exchanges, and the generic rescattering diagram that includes intermediate meson M_i and baryon B_i states.

$M_i B_i \rightarrow \phi p$, respectively. E_{M_i} and E_{B_i} designate the off-mass-shell energies in the intermediate meson and baryon states as shown in the third diagram of Fig. 1: $E_{M_i} = \sqrt{m_{M_i}^2 + |\boldsymbol{q}|^2}$ and $E_{B_i} = \sqrt{m_{B_i}^2 + |\boldsymbol{q}|^2}$, with the off-mass-shell three-momentum $\boldsymbol{q}$. s denotes a Mandelstam variable, i.e. the square of the total energy, $s = (E_\gamma + E_p)^2$. The second term of Eq. (1) corresponds to the third diagram of Fig. 1. In fact, it is quite involved to solve Eq. (1) in a full coupled-channel formalism. Instead, we will concentrate on the imaginary part of Eq. (1), which can be obtained by using the two-body unitarity relation. It is much simpler than solving Eq. (1) directly, since we only need the on-shell amplitudes $\mathcal{M}_{\gamma N \rightarrow M_i B_i}$ and $\mathcal{M}_{M_i B_i \rightarrow \phi N}$. Of course, the price we have to pay is to ignore the real contributions, which may be equally as important as the imaginary ones. However, as will be shown soon, this approximation already conveys significant information on how these coupled-channel effects are essential.

2.1. Pomeron exchange

The amplitude of the Pomeron exchange [15–17] corresponding to the first diagram of Fig. 1 is given by

$$\mathcal{M} = -\bar{u}(p_2)\mathcal{M}_{\mu\nu}u(p_1)\epsilon_\phi^{*\mu}\epsilon_\gamma^\nu, \tag{2}$$

where ϵ_ϕ and ϵ_γ are the polarization vectors of the ϕ meson and photon, respectively. $\mathcal{M}_{\mu\nu}$ is

$$\mathcal{M}^{\mu\nu} = M(s,t)\Gamma^{\mu\nu}, \tag{3}$$

where the transition operator $\Gamma^{\mu\nu}$ is defined as

$$\Gamma^{\mu\nu} = k\!\!\!/_\gamma \left(g^{\mu\nu} - \frac{p_3^\mu p_3^\nu}{p_3^2} \right) - \gamma^\nu \left(k_\gamma^\mu - p_3^\mu \frac{k_1 \cdot p_3}{p_3^2} \right) - \left(p_3^\nu - \bar{p}^\nu \frac{k_\gamma \cdot p_3}{\bar{p} \cdot k_1} \right) \left(\gamma^\mu - \frac{p\!\!\!/_3 p_3^\mu}{p_3^2} \right), \tag{4}$$

with $\bar{p} = (p_1 + p_2)/2$. Note that the Pomeron amplitude preserves gauge invariance $k_1^\nu \mathcal{M}_{\mu\nu} = 0$. The corresponding invariant amplitude $M(s,t)$ in Eq. (3) is written as

$$M(s,t) = C_p F_N(t) F_\phi(t) \left(\frac{s}{s_p} \right)^{\alpha_p(t)-1} \exp\left(-\frac{i\pi}{2}\alpha_p(t) \right) R(E), \tag{5}$$

where $s = (k_1 + p_1)^2$ and $t = (k_1 - k_2)^2$. $F_N(t)$ is the isoscalar form factor of the nucleon, whereas $F_\phi(t)$ is the form factor for the photon–ϕ meson–Pomeron vertex. They are parameterized, respectively, as

$$F_N(t) = \frac{4M_N^2 - a_N^2 t}{(4M_N^2 - t)(1 - t/t_0)^2},$$

$$F_\phi(t) = \frac{2\mu_0^2}{(1 - t/M_\phi^2)(2\mu_0^2 + M_\phi^2 - t)}. \tag{6}$$

The Pomeron trajectory $\alpha_p(p) = 1.08 + 0.25\,t$ in Eq. (5) is determined from hadron elastic scattering in the high-energy regime, and $s_p = 4\,\text{GeV}^2$. The prefactor C_p in Eq. (5) governs the overall strength of the amplitude and is given by $C_p = 0.7566$, as in Ref. [8]. Since the Pomeron exchange is in fact the main contribution in the high-energy regime, while the production mechanism at low energies should be explained by hadronic degrees of freedom, we introduce a phenomenological factor $R(E)$ to suppress the Pomeron effects. It is plausible, because it still keeps all the important

high-energy behavior of the Pomeron exchage. The factor $R(E)$ is given as

$$R(E) = 1 - \exp[-(E - E_{\text{th}})^3], \tag{7}$$

where E_{th} is the threshold energy of ϕ photoproduction.

2.2. π and η exchanges

To calculate pseudoscalar meson ($\varphi = \pi^0, \eta$) exchange in the t channel (the second diagram of Fig. 1), we introduce the following effective Lagrangians:

$$\mathcal{L}_{\phi\gamma\varphi} = \frac{e}{m_\phi} g_{\phi\gamma\varphi} \epsilon^{\mu\nu\alpha\beta} \partial_\mu \phi_\nu \partial_\alpha A_\beta \varphi,$$

$$\mathcal{L}_{\varphi NN} = \frac{g_{\varphi NN}}{2M_N} \bar{N} \gamma_\mu \gamma_5 N \partial^\mu \varphi, \tag{8}$$

where ϕ_ν, A_β, and N denote the ϕ vector meson, photon, and nucleon fields, respectively. m_ϕ and M_N stand for the ϕ meson and nucleon masses respectively. e represents the electric charge. The t-channel amplitude then takes the following form:

$$\mathcal{M} = \frac{e g_{\varphi NN} g_{\phi\gamma\varphi}}{m_\phi} \frac{i F_{\varphi NN}(t) F_{\phi\gamma\varphi}}{t - M_\varphi^2} \bar{u}(p_2)(\not{k}_1 - \not{k}_2)\gamma_5 u(p_1) \epsilon^{\mu\nu\alpha\beta} k_{2\mu} \epsilon^*_{\phi\nu} k_{1\alpha} \epsilon_{\gamma\beta}, \tag{9}$$

where r is the four-momentum of an exchanged pseudoscalar meson. We introduce the monopole-type form factors for each vertex $F_{\varphi NN}(t)$ and $F_{\phi\gamma\varphi}$, defined as

$$F_{\varphi NN}(t) = \frac{\Lambda_{\varphi NN}^2 - M_\varphi^2}{\Lambda_{\varphi NN}^2 - t}, \quad F_{\phi\gamma\varphi}(t) = \frac{\Lambda_{\phi\gamma\varphi}^2 - M_\varphi^2}{\Lambda_{\phi\gamma\varphi}^2 - t}. \tag{10}$$

For the coupling constants and the cut-off masses for the pseudoscalar exchange, we follow Ref. [5]: $g_{\pi NN} = 13.26$, $g_{\eta NN} = 3.527$ for the πNN and ηNN coupling constants, respectively. The cut-off masses are taken to be $\Lambda_{\pi NN} = 0.7\,\text{GeV}$ and $\Lambda_{\eta NN} = 1\,\text{GeV}$. Though these values are somewhat different from the phenomenological nucleon–nucleon potentials [18,19], the effects of the pseudoscalar meson exchanges on ϕ photoproduction are rather small. Thus, we will take the values given above typically used in ϕ photoproduction. Those of the coupling constants for the $\phi\gamma\varphi$ vertices are determined by using the radiative decays of the ϕ meson to π and η. Using the data from the Particle Data Group (PDG) [7], one can find $g_{\phi\gamma\pi} = -0.141$ and $g_{\phi\gamma\eta} = -0.707$. The negative signs of these coupling constants were determined by the phase conventions in SU(3) symmetry as well as by π photoproduction [5]. We choose the cut-off masses for the $\phi\gamma\pi$ and $\phi\gamma\eta$ form factors as follows: $\Lambda_{\phi\gamma\pi} = 0.77\,\text{GeV}$ and $\Lambda_{\phi\gamma\eta} = 0.9\,\text{GeV}$, respectively.

2.3. $K^+\Lambda(1520)$ rescattering effects

In addition to the Pomeron and pseudoscalar meson exchanges, we need to consider the seven different rescattering amplitudes. However, the corresponding transition processes $M_i B_i \rightarrow \phi p$ are not well known phenomenologically. Thus, we construct the seven different rescattering amplitudes with the Born approximation for simplicity: ρN, ωN, σN, πN, $K\Lambda(1116)$, $K^*\Lambda(1116)$, and $K\Lambda(1520)$, based on the effective Lagrangians. Since the $K\Lambda(1520)$ rescattering amplitude is the most significant among several possiblities in describing ϕ photoproduction, we first discuss the $K^+\Lambda(1520)$ one and then deal with all the other rescattering ones in the next subsection. The $\gamma N \rightarrow K^+\Lambda(1520)$ process was investigated within an effective Lagrangian method in Ref. [9], with results in good

Table 1. The strong coupling constants and anomalous magnetic moments used in the present work.

$g_{KN\Lambda^*}$	11	Ref. [9]
$g_{\phi KK}$	4.7	Ref. [7]
$g_{\phi NN}$	0.25	Ref. [21]
κ_p	1.79	Ref. [7]
κ_ϕ	0.2	Ref. [21]

agreement with the experimental data. Thus, we will employ the formalism developed in Ref. [9] so that we may take into account the $K\Lambda(1116)$ coupled-channel effects more realistically.

The effective Lagrangians for $\gamma N \to K^+\Lambda(1520)$ are written as

$$\mathcal{L}_{KN\Lambda^*} = \frac{g_{KN\Lambda^*}}{M_K}\bar{N}\gamma_5\partial_\mu K^+\Lambda^{*\mu},$$

$$\mathcal{L}_{\phi KN\Lambda^*} = -\mathrm{i}\frac{g_{KN\Lambda^*}}{M_K}g_{\phi KK}\bar{N}\gamma_5\phi_\mu K^+\Lambda^{*\mu},$$

$$\mathcal{L}_{\phi KK} = -\mathrm{i}g_{\phi KK}(\partial^\mu K^- K^+ - \partial^\mu K^+ K^-)\phi_\mu,$$

$$\mathcal{L}_{\phi NN} = -g_{\phi NN}\bar{N}\left[\gamma_\mu\phi^\mu - \frac{\kappa_\phi}{2M_N}\sigma^{\mu\nu}\partial_\nu\phi_\mu\right]N,$$

$$\mathcal{L}_{\gamma KK} = -\mathrm{i}e(\partial^\mu K^- K^+ - \partial^\mu K^+ K^-)A_\mu,$$

$$\mathcal{L}_{\gamma NN} = -e\bar{N}\left[\gamma^\mu - \frac{\kappa_N}{2M_N}\sigma^{\mu\nu}\partial_\nu\right]A_\mu N,$$

$$\mathcal{L}_{\gamma KN\Lambda^*} = -\mathrm{i}\frac{eg_{KN\Lambda^*}}{M_K}\bar{N}\gamma_5 A_\mu K^+\Lambda^{*\mu}, \tag{11}$$

where K and $\Lambda^{*\mu}$ denote the K meson and $\Lambda(1520)$ fields, respectively. For $\Lambda(1520)$, we utilize the Rarita–Schwinger formalism. M_K is the kaon mass. The $KN\Lambda^*$ coupling constant is taken from Ref. [9], since we use the amplitude derived there. The ϕKK coupling constant can be determined from the experimental data for the decay width $\Gamma_{\phi\to KK}$. On the other hand, $g_{\phi NN}$ is not well known experimentally. Recent experiments measuring the strange vector form factors imply that the strange quark gives almost no contribution to the nucleon electromagnetic (EM) form factors [1]. One can deduce from this experimental fact that the ϕNN coupling constant should be very small. In Ref. [21], the ϕNN was estimated by using a microscopic hadronic model with $\pi\rho$ continuum: $g_{\phi NN} = \pm 0.25$ and $\kappa_\phi = 0.2$, which are compatible with the recent data for the strange vector form factors. Thus, we will take these values in the present work. However, note that the s-channel contribution with the ϕNN vertex is almost negligible. In Table 1, the relevant strong coupling constants and anomalous magnetic moments are listed.

Based on the effective Lagrangians given in Eq. (11), we can write down the amplitude for the $K^+\Lambda^*(1520)$ rescattering equation, Eq. (1). As mentioned previously, it is rather complicated to solve the BbS equation (1). Thus, instead of dealing with Eq. (1) directly, we will use the two-body unitarity relation to further select the imaginary part of Eq. (1). This is in fact identical to using the Landau–Cutkosky rule [12,13]. Knowing the singularities and the cuts of the invariant amplitudes, and utilizing the two-body unitarity, we can easily obtain the imaginary part of the invariant amplitudes. Having computed the Lorentz-invariant phase space volume factors, we obtain the imaginary
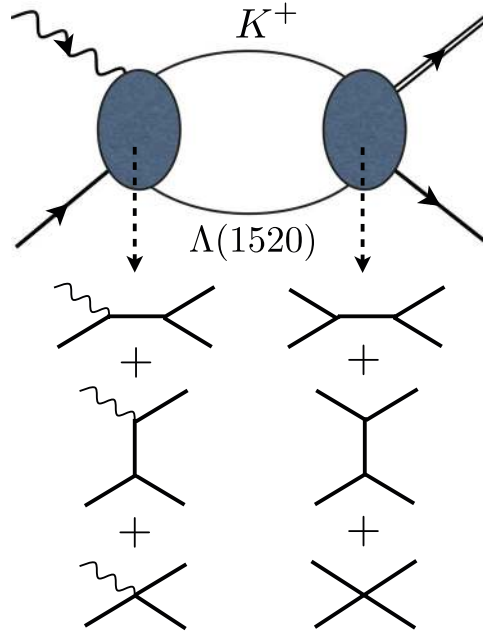
Fig. 2. Feynman diagrams for the $K^+\Lambda(1520)$ rescattering. The form factors are introduced in a gauge-invariant way.

part of the amplitude as

$$\mathrm{Im}\,\mathcal{M}_{K^+\Lambda^*\mathrm{rescatt.}} = -\frac{1}{8\pi}\frac{r}{\sqrt{s}}\int\frac{d\Omega}{4\pi}\mathcal{M}_L(\gamma p \to K^+\Lambda^*)\mathcal{M}_R^\dagger(K^+\Lambda^* \to \phi p), \qquad (12)$$

where r is the magnitude of the K^+ on-mass-shell three-momentum. This imaginary part of the amplitude is schematically drawn in Fig. 2. The shaded ellipse on the left-hand side represents the invariant amplitude for $\gamma p \to K^+\Lambda^*$, which is basically the same as that of Ref. [9] except for different form factors, as will be explained later. It consists of three different types of the Feynman diagrams as shown below the left dashed arrow. On the other hand, the right ellipse stands for the $K^+\Lambda^* \to \phi p$ process that contains the diagrams below the right arrow, generically. Note that we use a similar method as in Ref. [8] but we choose different form factors and parameters. The corresponding invariant amplitudes $\mathcal{M}_L(\gamma p \to K^+\Lambda^*)$ and $\mathcal{M}_R(K^+\Lambda^* \to \phi p)$ with the form factors are defined as follows:

$$\mathcal{M}_L(\gamma p \to K^+\Lambda^*) = (\mathcal{M}_{L,s} + \mathcal{M}_{L,t} + \mathcal{M}_{L,c})F_L(s,t),$$
$$\mathcal{M}_R(K^+\Lambda^* \to \phi p) = (\mathcal{M}_{R,s} + \mathcal{M}_{R,t} + \mathcal{M}_{R,c})F_R(s,t), \qquad (13)$$

where $\mathcal{M}_{L,s}$ ($\mathcal{M}_{R,s}$), $\mathcal{M}_{L,t}$ ($\mathcal{M}_{R,t}$), and $\mathcal{M}_{L,c}$ ($\mathcal{M}_{R,c}$) represent the s-channel, the t-channel, and the contact-term contributions to the $\gamma p \to K^+\Lambda^*$ ($K^+\Lambda^* \to \phi p$) process, respectively:

$$\mathcal{M}_{L,s} = \frac{eg_{KN\Lambda^*}}{M_K}\bar{u}^\mu k_{2\mu}\gamma_5 \frac{\slashed{k}_1 + \slashed{q} + M_N}{q^2 - M_N^2}\slashed{\epsilon}u(p_1)$$
$$+ \frac{e\kappa_p g_{KN\Lambda^*}}{2M_N M_K}\bar{u}^\mu k_{2\mu}\gamma_5\frac{\slashed{q} + M_N}{q^2 - M_p^2}\slashed{\epsilon}\slashed{k}_1 u(p_1),$$

Table 2. Cut-off parameters used in Eq. (13)

n_1	6
n_2	2
n_3	1
n_4	1
Λ_1	1.59 GeV
Λ_2	0.65 GeV
Λ_3	1.5 GeV
Λ_4	1.5 GeV

$$\mathcal{M}_{L,t} = -\frac{2eg_{KN\Lambda^*}}{M_K}\bar{u}^\mu\gamma_5 u(p_1)\frac{q_K^\mu}{t_K - M_K^2},$$

$$\mathcal{M}_{L,c} = \frac{eg_{KN\Lambda^*}}{M_K}\bar{u}^\mu\epsilon_\mu\gamma_5 u(p_1),$$

$$\mathcal{M}_{R,s} = -\mathrm{i}\frac{g_{KN\Lambda^*}g_{\phi NN}}{M_K}\bar{u}(p_2)\;\slashed{\epsilon}_\phi^*\frac{\slashed{q}+M_p}{q^2-M_p^2}\gamma_5 k_1^\alpha u^\alpha(p_1)$$

$$+\mathrm{i}\frac{g_{KN\Lambda^*}g_{\phi NN}}{M_K}\frac{\kappa_\phi}{2M_p}\bar{u}(p_2)\;\slashed{k}_2\;\slashed{\epsilon}_\phi^*\frac{\slashed{q}+M_p}{q^2-M_p^2}\gamma_5 k_1^\alpha u^\alpha(p_1),$$

$$\mathcal{M}_{R,t} = -\frac{\mathrm{i}g_{KN\Lambda^*}g_{\phi KK}}{M_K}\frac{2k_1\cdot\epsilon_\phi^*}{q_K^2-M_K^2}\bar{u}(p_2)\gamma_5 q_t^\alpha u^\alpha(p_1),$$

$$\mathcal{M}_{R,c} = -\frac{\mathrm{i}g_{KN\Lambda^*}g_{KNN}}{M_K}\bar{u}(p_2)\gamma_5\epsilon_\phi^{*\mu}u^\mu(p_1). \tag{14}$$

We introduce the form factors $F_R(s,t)$ and $F_L(s,t)$ for $\mathcal{M}_R$ and $\mathcal{M}_L$, respectively, in particular, in a gauge-invariant manner for the $\gamma p \to K^+\Lambda^*$ rescattering:

$$F_R(s,t) = \left[\frac{n_1\Lambda_1^4}{n_1\Lambda_1^4+(s-M_p^2)^2}\right]^{n_1}\left[\frac{n_2\Lambda_2^4}{n_2\Lambda_2^4+t^2}\right]^{n_2},$$

$$F_L(s,t) = \left[\frac{n_3\Lambda_3^4}{n_3\Lambda_3^4+(s-M_p^2)^2}\right]^{n_3}\left[\frac{n_4\Lambda_4^4}{n_4\Lambda_4^4+t^2}\right]^{n_4}, \tag{15}$$

where the cut-off masses Λ_i and powers n_i are fitted to the experimental data for $\gamma p \to K^+\Lambda^*$ and $\gamma p \to \phi p$, which are listed in Table 2. In Fig. 3, we draw the numerical result of the total cross section for $\gamma p \to K^+\Lambda^*$ in comparison with the experimental data taken from Ref. [23]. It is in good agreement with the data.

2.4. All other rescattering amplitudes

In the same manner as done for the $K^+\Lambda^*$ rescattering amplitude, we consider the six different amplitudes, i.e. ρN, ωN, σN, πN, $K\Lambda(1116)$, and $K^*\Lambda(1116)$. ρ photoproduction has been studied theoretically in Refs. [11,24–26], in which the contributions of the t-channel π and σ exchanges were considered and σ exchange was found to be the dominant one, since it selects the isovector part of the EM current. Thus, we compute $\mathcal{M}_{\gamma p \to \rho p}$ and $\mathcal{M}_{\rho p \to \phi p}$ with the σ and π exchanges in the t-channel, respectively. We will show later, in Fig. 5, that indeed the σ exchange describes well, qualitatively, the $\gamma p \to \rho p$ reaction. In Ref. [24], ω photoproduction was also discussed within the same framework. In contrast to the $\gamma p \to \rho p$ reaction, the π exchange appeared to be dominant,
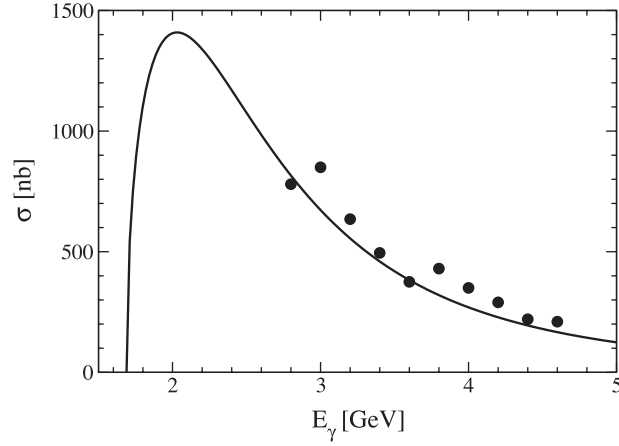
Fig. 3. Total cross section of the $\gamma p \to K \Lambda(1520)$ reaction as compared to the experimental data [23].

since it picks up the isoscalar part of the EM current. Correspondingly, we consider the ωp rescattering contribution, where ω is produced by the one pion exchange. The σp and πp rescattering amplitudes are obtained by reversing the ρp and ωp rescattering diagrams. The $\gamma p \to K \Lambda(1116)$ and $\gamma p \to K^* \Lambda(1116)$ reactions were measured by several experimental collaborations [27–32] and were investigated theoretically [33–37]. While we consider all the relevant diagrams for the $K \Lambda^*(1520)$ rescattering contribution because of its significance, we will take into account only the K-exchange diagrams in the t-channel for the $K \Lambda$ and $K^* \Lambda$ rescattering diagrams, since these two rescattering diagrams turn out to have tiny effects on ϕ photoproduction.

The relevant effective Lagrangians for these rescattering diagrams are given as follows:

$$\mathcal{L}_{\gamma\rho\sigma} = \frac{g_{\gamma\rho\sigma}}{m_\rho}[\partial_\mu A_\nu \partial^\mu \rho^\nu - \partial_\mu A_\nu \partial^\nu \rho^\mu]\sigma,$$

$$\mathcal{L}_{\sigma NN} = g_{\sigma NN}\bar{N}N\sigma,$$

$$\mathcal{L}_{\pi^0 NN} = -\mathrm{i}g_{\pi NN}\bar{N}\gamma_5 \tau_3 N\pi^0,$$

$$\mathcal{L}_{\pi\rho\phi} = \frac{g_{\pi\rho\phi}}{m_\phi}\epsilon_{\mu\nu\alpha\beta}\partial^\nu \phi^\mu \partial^\beta \rho^\alpha \pi_0,$$

$$\mathcal{L}_{\omega\phi\sigma} = \frac{g_{\omega\phi\sigma}}{m_\phi}(\partial_\mu \omega_\nu \partial^\mu \phi^\nu - \partial_\mu \omega_\nu \partial^\nu \phi^\mu),$$

$$\mathcal{L}_{\gamma\omega\pi} = \frac{g_{\gamma\omega\pi}}{m_\omega}\epsilon_{\mu\nu\alpha\beta}\partial^\nu A^\mu \partial^\beta \omega^\alpha \pi^0,$$

$$\mathcal{L}_{VNN} = -g_{VNN}\bar{N}\left(\gamma_\mu V^\mu - \frac{\kappa_V}{2M_N}\sigma^{\mu\nu}\partial_\nu V_\mu\right)N, \quad (V = \omega, \, \rho),$$

$$\mathcal{L}_{\gamma KK} = -\mathrm{i}e\left[(\partial^\mu K^+)K^- - (\partial^\mu K^-)K^+\right]A_\mu,$$

$$\mathcal{L}_{\phi KK} = \mathrm{i}g_{\phi KK}\left[(\partial^\mu K^+)K^- - (\partial^\mu K^-)K^+\right]\phi_\mu,$$

$$\mathcal{L}_{KN\Lambda} = -\mathrm{i}g_{KP\Lambda}\bar{\Lambda}\gamma_5 N K^-,$$

$$\mathcal{L}_{\gamma KK^*} = \frac{g_{\gamma KK^*}}{m_{K^*}}\epsilon_{\mu\nu\alpha\beta}\partial^\nu A^\mu \partial^\beta K^{*\alpha} K,$$

$$\mathcal{L}_{\phi KK^*} = \frac{g_{\phi KK^*}}{m_\phi}\epsilon_{\mu\nu\alpha\beta}\partial^\nu \phi^\mu \partial^\beta K^{*\alpha} K, \tag{16}$$

Table 3. Coupling constants and cut-off masses used in rescattering amplitudes

$g_{\gamma\rho\sigma}$	0.82	Ref. [24]
$g_{\sigma NN}$	10.026	Ref. [24]
$g_{\pi NN}$	13.26	Ref. [24]
$g_{\pi\rho\phi}$	-1.258	Ref. [7]
$g_{\phi\omega\sigma}$	-0.45	Ref. [7]
$g_{\gamma\omega\pi}$	0.557	Ref. [7]
$g_{\omega NN}$	10.35	Ref. [20]
$g_{\rho NN}$	3.72	Ref. [20]
$g_{\phi KK}$	4.48	Ref. [7]
$g_{KN\Lambda}$	-13.26	Ref. [38]
$g_{\gamma KK^*}$	$0.254\,\text{GeV}^{-1}$	Ref. [7]
$g_{\phi KK^*}$	10.74	Refs. [7,39]
κ_ω	0	Ref. [20]
κ_ρ	6.1	Ref. [40]
$\Lambda_{\pi\rho\phi}$	$1.05\,\text{GeV}$	Ref. [17]
$\Lambda_{\pi NN}$	$1.05\,\text{GeV}$	Ref. [17]
$\Lambda_{\gamma\rho\sigma}$	$1.05\,\text{GeV}$	Ref. [24]
$\Lambda_{\sigma NN}$	$1.1\,\text{GeV}$	Ref. [24]
Λ_σ	$1\,\text{GeV}$	Ref. [24]
$\Lambda_{\sigma\rho\rho}$	$0.9\,\text{GeV}$	Ref. [24]
$\Lambda_{\sigma\omega\phi}$	$0.9\,\text{GeV}$	Ref. [7]
$\Lambda_{\pi\gamma\omega}$	$0.6\,\text{GeV}$	Ref. [20]
Λ_V	$1.227\,\text{GeV}$	Ref. [41]
Λ_K	$1\,\text{GeV}$	

where the coupling constants and the cut-off masses are listed in Table 3. The invariant amplitudes for these diagrams are derived as follows:

$$\mathcal{M}_{1,L} = \frac{g_{\gamma\rho\sigma}g_{\sigma NN}}{M_\rho(t_\sigma - M_\sigma^2)}\left[(k_1 \cdot r)(\epsilon_\gamma \cdot \epsilon_\rho^*) - (k_1 \cdot \epsilon_\rho^*)(\epsilon_\gamma \cdot r)\right]\bar{u}(q)u(p_1)$$

$$\left\{\frac{\Lambda_{\gamma\rho\sigma}^2 - M_\sigma^2}{t_\sigma - M_\sigma^2} \cdot \frac{\Lambda_{\sigma NN}^2 - M_\sigma^2}{t_\sigma - M_\sigma^2}\right\},$$

$$\mathcal{M}_{1,R} = \frac{-ig_{\phi\rho\pi}g_{\pi NN}}{M_\phi(t_\pi - M_\pi^2)}\epsilon_{\mu\nu\alpha\beta}\epsilon_\phi^{*\mu}k_2^\nu\epsilon_\rho^\alpha r^\beta \bar{u}(p_2)\gamma_5 u(q) \times \left\{\frac{\Lambda_{\phi\rho\pi}^2 - M_\pi^2}{t_\pi - M_\pi^2} \cdot \frac{\Lambda_{\pi NN}^2 - M_\sigma^2}{t_\pi - M_\pi^2}\right\},$$

$$\mathcal{M}_{2,L} = \frac{-ig_{\gamma\omega\pi}g_{\pi NN}}{M_\omega(t_\pi - M_\pi^2)}\epsilon_{\mu\nu\alpha\beta}\epsilon_\gamma^\mu k_1^\nu\epsilon_\omega^{*\alpha} r^\beta \bar{u}(q)\gamma_5 u(p_1) \times \left\{\frac{\Lambda_{\gamma\omega\pi}^2 - M_\pi^2}{t_\pi - M_\pi^2} \cdot \frac{\Lambda_{\pi NN}^2 - M_\pi^2}{t_\pi - M_\pi^2}\right\},$$

$$\mathcal{M}_{2,R} = \frac{-ig_{\phi\omega\sigma}g_{\sigma NN}}{M_\phi(t_\sigma - M_\sigma^2)}\bar{u}(p_2)u(q)\left[(r \cdot k_2)(\epsilon_\omega \cdot \epsilon_\phi^*) - (r \cdot \epsilon_\phi^*)(k_2 \cdot \epsilon_\omega)\right]$$

$$\times \left\{\frac{\Lambda_{\phi\omega\sigma}^2 - M_\sigma^2}{t_\sigma - M_\sigma^2} \cdot \frac{\Lambda_{\sigma NN}^2 - M_\sigma^2}{t_\sigma - M_\sigma^2}\right\},$$

$$\mathcal{M}_{3,L} = \frac{g_{\rho NN}g_{\gamma\rho\sigma}}{M_\rho(t_\rho - M_\rho^2)}\left[k_1^\alpha(\epsilon_\gamma \cdot r) - \epsilon_\gamma^\alpha(k_1 \cdot r)\right]\bar{u}(p_2)\left[\gamma_\alpha(1 + \kappa_\rho) - \frac{\kappa_\rho}{M_p}q^\alpha\right]u(p_1)$$

$$\times \left\{\left(\frac{\Lambda_\rho^2}{\Lambda_\rho^2 - (\boldsymbol{k}_1 - r)^2}\right)^2\right\},$$

$$\mathcal{M}_{3,R} = \frac{g_{\omega NN} g_{\phi\omega\sigma}}{M_\phi(t_\omega - M_\omega^2)} \Big[(r \cdot \epsilon_\phi^*) k_2^\mu - (r \cdot k_2 - M_\phi^2) \epsilon_\phi^{*\mu} \Big]$$

$$\times \bar{u}(p_1) \Big[\gamma_\mu(1 + \kappa_\omega) - \frac{\kappa_\omega}{2M_p} q_\mu \Big] u(q) \left\{ \left(\frac{\Lambda_\omega^2}{\Lambda_\omega^2 - (r - k_2)^2} \right)^2 \right\},$$

$$\mathcal{M}_{4,L} = \frac{-g_{\omega NN} g_{\gamma\omega\pi}}{M_\omega(t_\omega - M_\omega^2)} \epsilon_{\mu\nu\alpha\beta} \epsilon_\gamma^\mu k_1^\nu r^\beta \bar{u}(q) \Big[\gamma^\alpha(1 + \kappa_\omega) - \frac{\kappa_\omega}{M_P} q^\alpha \Big] u(p_1)$$

$$\times \left\{ \left(\frac{\Lambda_\omega^2}{\Lambda_\omega^2 - (r - k_2)^2} \right)^2 \right\},$$

$$\mathcal{M}_{4,R} = \frac{-g_{\rho NN} g_{\phi\rho\pi}}{M_\phi(t_\rho - M_\rho^2)} \epsilon_{\mu\nu\alpha\beta} \epsilon_\phi^{*\mu} k_2^\nu r^\beta \bar{u}(p_2) \Big[\gamma^\alpha(1 + \kappa_\rho) - \frac{\kappa_\rho}{M_N} q l^\alpha \Big] u(q),$$

$$\times \left\{ \left(\frac{\Lambda_\rho^2}{\Lambda_\rho^2 - (k_1 - r)^2} \right)^2 \right\},$$

$$\mathcal{M}_{5,L} = \frac{-2ie g_{KP\Lambda}}{(t_L - M_K^2)} (r \cdot \epsilon_\gamma) \bar{u}(q) \gamma_5 u(p_1) \times \left\{ \left(\frac{\Lambda_K^2 - M_K^2}{t_K - M_K^2} \right)^2 \right\},$$

$$\mathcal{M}_{5,R} = \frac{2i g_{\phi KK} g_{KP\Lambda}}{(t_R^2 - M_K^2)} (r \cdot \epsilon_\phi^*) \bar{u}(p_2) \gamma_5 u(q) \times \left\{ \left(\frac{\Lambda_K^2 - M_K^2}{t_K - M_K^2} \right)^2 \right\},$$

$$\mathcal{M}_{6,L} = \frac{-i g_{\gamma KK^*} g_{KP\Lambda}}{M_{K^*}(t_L - M_K^2)} \epsilon_{\mu\nu\alpha\beta} \epsilon_{\gamma\mu} k_1^\nu \epsilon_{K*}^\alpha r^\beta \bar{u}(q) \gamma_5 u(p_1) \times \left\{ \left(\frac{\Lambda_K^2 - M_K^2}{\Lambda_K^2 - t_K} \right)^2 \right\},$$

$$\mathcal{M}_{6,R} = \frac{i g_{\phi KK^*} g_{KP\Lambda}}{M_\phi(t_R - M_K^2)} \epsilon_{\mu\nu\alpha\beta} \epsilon_\phi^{*\mu} k_2^\nu \epsilon_{K*}^\alpha r^\beta \bar{u}(p_2) \gamma_5 u(q) \times \left\{ \left(\frac{\Lambda_K^2 - M_K^2}{\Lambda_K^2 - t_K} \right)^2 \right\}, \tag{17}$$

where the subscripts $1, \ldots, 6$ correspond to the rescattering amplitudes. The other subscripts L and R denote the $\gamma p \to MB$ and $MB \to \phi p$ parts, respectively. In Figs. 4 and 5 we draw the results of the total cross sections for the $\gamma p \to \rho p$ and $\gamma p \to \omega p$ reactions, respectively. The results are qualitatively in agreement with the experimental data.

3. Numerical results and discussion

We are now in a position to discuss the numerical results for ϕ photoproduction. We start with the differential cross section at the forward angle $d\sigma/dt \, (\theta = 0)$ as a function of the photon energy E_γ in the laboratory frame. The parameters are determined in the following manner. We fix the cut-off parameters for the $K\Lambda^*(1520)$ box diagrams to describe the E_γ dependence of $d\sigma/dt$ in the lower energy region, in particular, to explain the well-known bump-like structure around $E_\gamma \approx 2.3\,\text{GeV}$. The parameters of all other hadronic diagrams are taken from existing references as explained in the previous section.

Figure 6 illustrates various contributions to $d\sigma/dt \, (\theta = 0)$ as a function of the photon energy E_γ from the Pomeron exchange, the t-channel π and η exchanges, and seven rescattering diagrams. The solid curve with symbol P draws the contribution of the Pomeron exchange to $d\sigma/dt$. As expected, it governs E_γ dependence in the higher energy region ($E_\gamma \geq 3\,\text{GeV}$). Note, however, that the Pomeron does not contribute to $d\sigma/dt$ below around $E_\gamma = 2.3\,\text{GeV}$ in the present work. The π
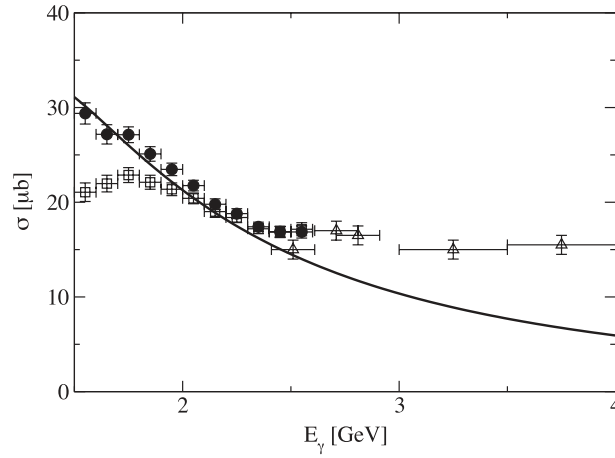
Fig. 4. Total cross section of the $\gamma p \rightarrow \rho^0 p$ reaction. The solid curve depicts the present result obtained from the t-channel σ exchange diagram. The closed circles and the open squares are taken from Ref. [42], whereas the open triangles are taken from Ref. [43].
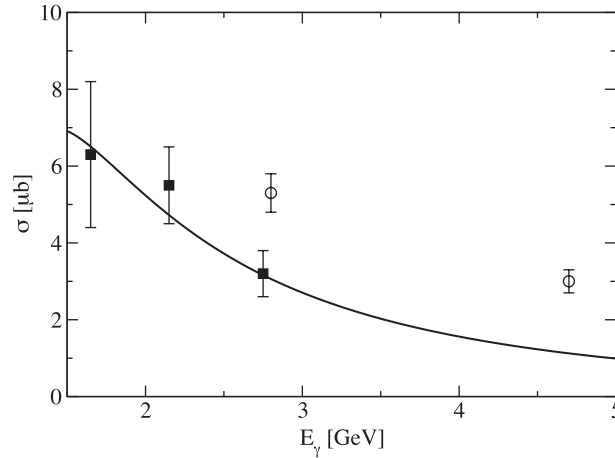
Fig. 5. Total cross section of the $\gamma p \rightarrow \omega p$ reaction. The solid curve depicts the present result obtained from the t-channel π exchange diagram. The closed squares denote the experimental data from Ref. [46], whereas the open circles represent those from Ref. [44].

and η exchanges provide a certain amount of effect on the differential cross section (solid curve with symbol T). The contribution of the π and η exchanges starts to increase from the threshold energy and then it decreases very slowly when it reaches approximately 3 GeV. Thus, the effects of the π and η exchanges are quite important in the lower E_γ energy region up to 3 GeV, where the Pomeron exchange overtakes the π and η exchanges.

Except for the $K\Lambda^*(1520)$ rescattering diagram, all other rescattering contributions turn out to be negligibly small. However, the $K\Lambda^*(1520)$ rescattering diagram plays an essential role in describing the experimental data for $d\sigma/dt$ in the lower E_γ region, in particular, explaining the bump-like structure near 2.3 GeV. In Fig. 7, we enlarge the results of Fig. 6 in the threshold region. This is very different from the conclusion of Ref. [8], where the $K\Lambda^*(1520)$ seems to be suppressed in the K-matrix formalism. The reason lies in the fact that we have considered the imaginary contribution of the coupled-channel effects through the unitarized rescattering equation (1) and have introduced different form factors for the $\gamma p \rightarrow K\Lambda^*$ and $K\Lambda^* \rightarrow \phi p$ reactions. In general, form factors are
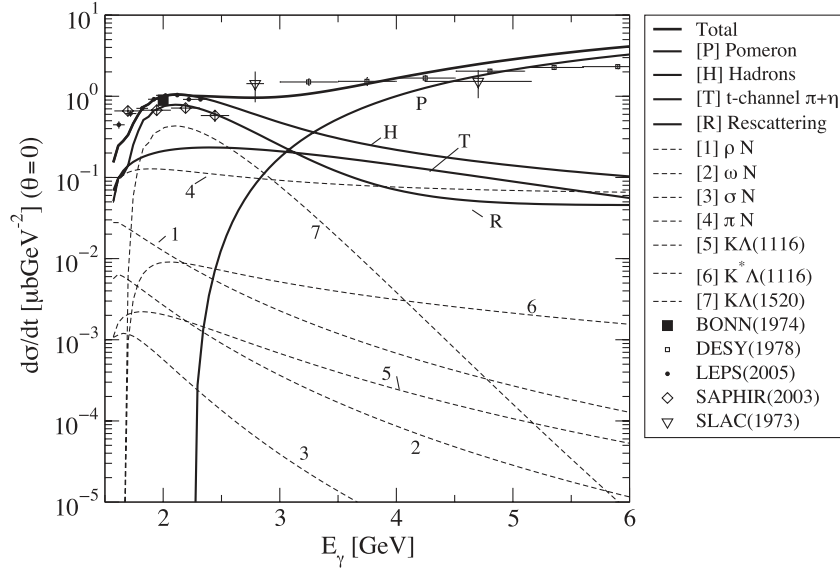
Fig. 6. Differential cross section as a function of the photon energy E_γ on a log scale. The thick solid curve depicts the result with all contributions included. The solid curves with the symbols P, T, B, and H represent the Pomeron contribution, those of π and η exchanges, those of all the box diagrams, and the total contribution of hadronic diagrams ($T + B$), respectively. The dashed curves with numbers in order denote the effects of the seven rescattering diagrams separately.
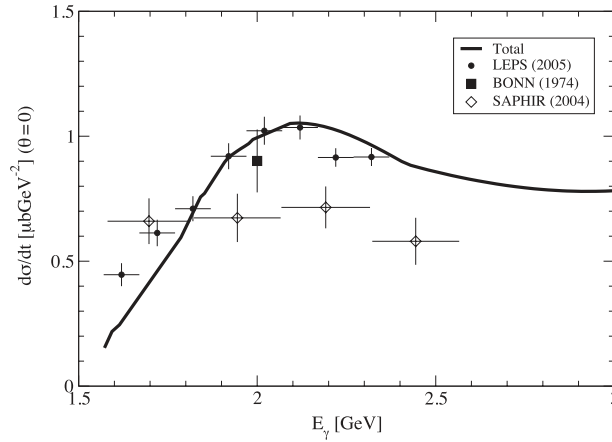

Fig. 7. The differential cross section as a function of the photon energy E_γ near the threshold on a linear scale.

given as functions of two Mandelstam variables for the rescattering diagrams, i.e. $F(s, t)$, since we have two off-shell particles in the s-channel and another two off-shell particles in the t-channel. However, it is very difficult to preserve the gauge invariance in the presence of the form factors. Thus, we have introduced a type of overall form factor to keep the gauge invariance in the $\gamma p \rightarrow K \Lambda^*$ part, as written in Eq. (13). To maintain consistency, we have also included a similar type of form factor in the $K \Lambda^* \rightarrow \phi p$ part. With these form factors considered, we find that the $K \Lambda^*$ rescattering diagram is indeed enhanced as shown in Fig. 6 in comparison with Ref. [8]. The contribution of the $K \Lambda^*$ rescattering diagram increases sharply up to $E_\gamma \approx 2$ GeV and then falls off linearly. The result of the $K \Lambda^*$ rescattering diagram indicates that the off-shell effects, which arise from the form factors and the rescattering equation, may come into play. Moreover, the form factors given in Eq. (13) are crucial in explaining the differential cross section as a function of θ which will be shown in Fig. 8.
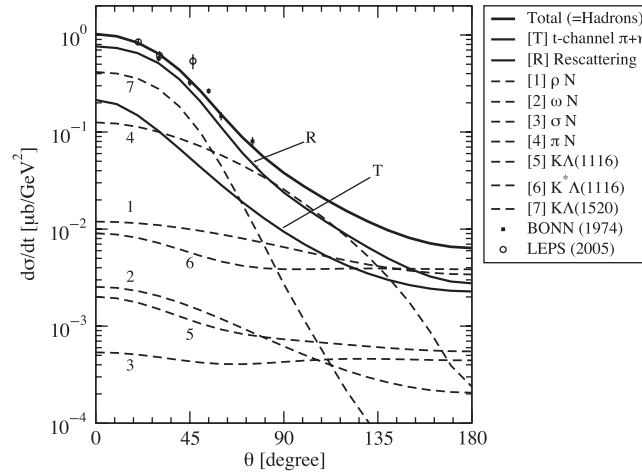
Fig. 8. The differential cross section as a function of the scattering angle θ with the photon energy at $E_\gamma = 2\,\text{GeV}$. The thick solid curve depicts the result with all hadronic contributions included. The solid curves with the symbols T and B represent the contribution of the π and η exchanges and those of all the box diagrams, respectively. The dashed curves with numbers in order denote the effects of the seven rescattering channels separately.

Another reason for the discrepancy may be due to fact that there is some inconsistency in Ref. [8]: the K-matrix formalism that was employed in Ref. [8] is only valid for real K, by definition. On the other hand, the Pomeron exchange provides only the imaginary amplitude. That is the reason why the sign had to be modified as mentioned in the erratum given in Ref. [8]. Moreover, the present way of treating the coupled-channel effects is rather different from Ref. [8].

Considering the fact that the $K^*\Lambda$ threshold energy ($E_{\text{th}} \approx 2\,\text{GeV}$) is very close to that of ϕ photo-production ($E_{\text{th}} \approx 1.96\,\text{GeV}$), one might ask why the contribution of the $K^*\Lambda$ is suppressed. While the $K\Lambda^*(1520)$ channel ($E_{\text{th}} \approx 2\,\text{GeV}$) is directly related to ϕp, since both are subreactions of the $\gamma p \to K\bar{K}p$ process, the $\gamma p \to K^*\Lambda$ reaction is distinguished from those two reactions, because the $K^*\Lambda$ channel is related to the $\gamma p \to \pi K\Lambda$ reaction. Thus, one can qualitatively understand why the contribution of the $K^*\Lambda$ rescattering diagrams is suppressed.

In Fig. 8, the differential cross section as a function of the scattering angle is depicted at $E_\gamma = 2\,\text{GeV}$. Since the Pomeron exchange is suppressed at this photon energy because of $s_{\text{th}} = 2.3\,\text{GeV}$, we can examine each hadronic contribution to the differential cross section in more detail. Figure 8 clearly shows that the $K\Lambda(1520)$ rescattering diagram is the most dominant among the hadronic contributions. Adding all the effects of the rescattering diagrams, we find that the rescattering contributions almost describe the θ dependence. Together with the π and η exchanges, the result of the differential cross section is in good agreement with the experimental data [4,45].

The differential cross section as a function the scattering angle is drawn in Fig. 9. The left and right panels correspond to the photon energies $E_\gamma = 3\,\text{GeV}$ and $3.7\,\text{GeV}$, respectively. As expected, the hadronic contribution is dominant over the Pomeron exchange at the lower photon energy, while at $E_\gamma = 3.7\,\text{GeV}$ the Pomeron governs the $\gamma p \to \phi p$ process. Interestingly, the effects of the rescattering diagrams, in particular the $K\Lambda^*(1520)$ one, turn out to be larger than those of the π and η exchanges, whereas the rescattering diagrams seem to be suppressed at higher photon energies. This implies that the $K\Lambda^*(1520)$ rescattering diagram influences ϕ photoproduction only in the vicinity of the threshold energy. Figure 10 depicts the results of the differential cross section as a function of $t + |t|_{\text{min}}$ with eight different photon energies, where $|t|_{\text{min}}$ is the minimum four-momentum transfer
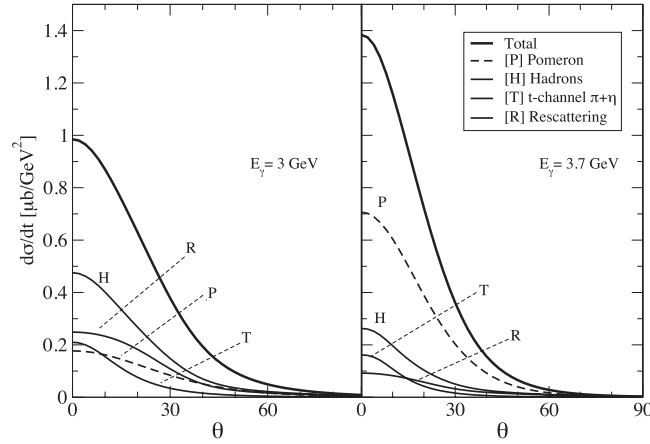
Fig. 9. The differential cross section as a function of the scattering angle θ with two different photon energies $E_\gamma = 3$ GeV and 3.7 GeV. The thick solid curve depicts the result with all contributions included. The solid curves with the symbols P, T, B, and H represent the Pomeron contribution, those of the π and η exchanges, those of all the rescattering diagrams, and the total contribution of hadronic diagrams ($T + B$), respectively.
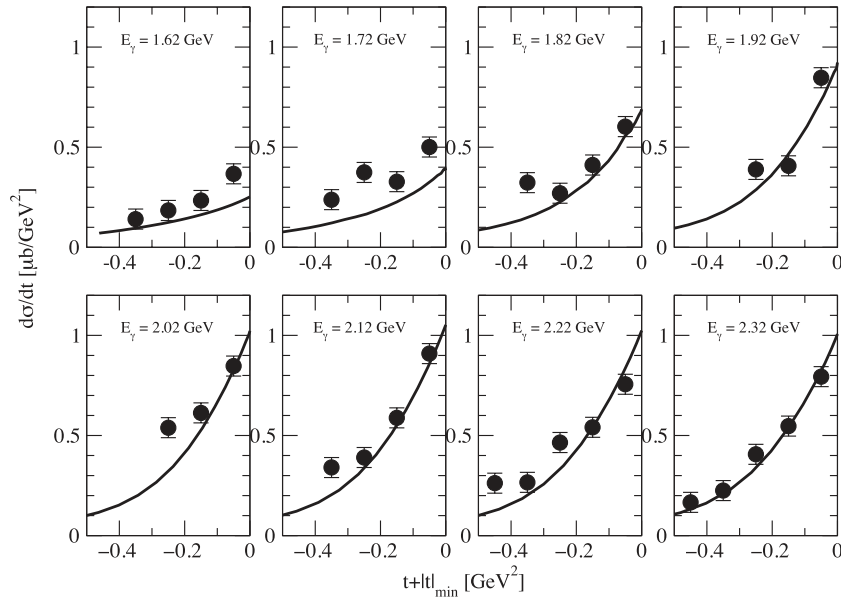

Fig. 10. Differential cross sections of the $\gamma p \to \phi p$ reaction as a function of $t + |t|_{\min}$ with eight different photon energies. The experimental data are taken from Ref. [4].

from the incident photon to the ϕ meson. The results are in good agreement with the experimental data taken from the measurement of the LEPS collaboration [4].

It is of great importance to examine the angular distribution of the $\phi \to K^+ K^-$ decay in the ϕ rest frame or in the Gottfried–Jackson (GJ) frame, since it makes the helicity amplitudes accessible to experimental investigation [47,48]. The detailed formalism for the angular distribution of the ϕ meson decay can be found in Refs. [5,48]. The decay angular distribution of ϕ photoproduction was measured at SAPHIR/ELSA [49], but the range of the photon energy is too wide. On the other hand, the LEPS collaboration measured the decay angular distribution at forward angles ($-0.2 < t + |t|_{\min}$) in two different energy regions: $1.97 < E_\gamma < 2.17$ GeV and $2.17 < E_\gamma < 2.37$ GeV [4], which are related to the energy around the local maximum of the cross section and that above the
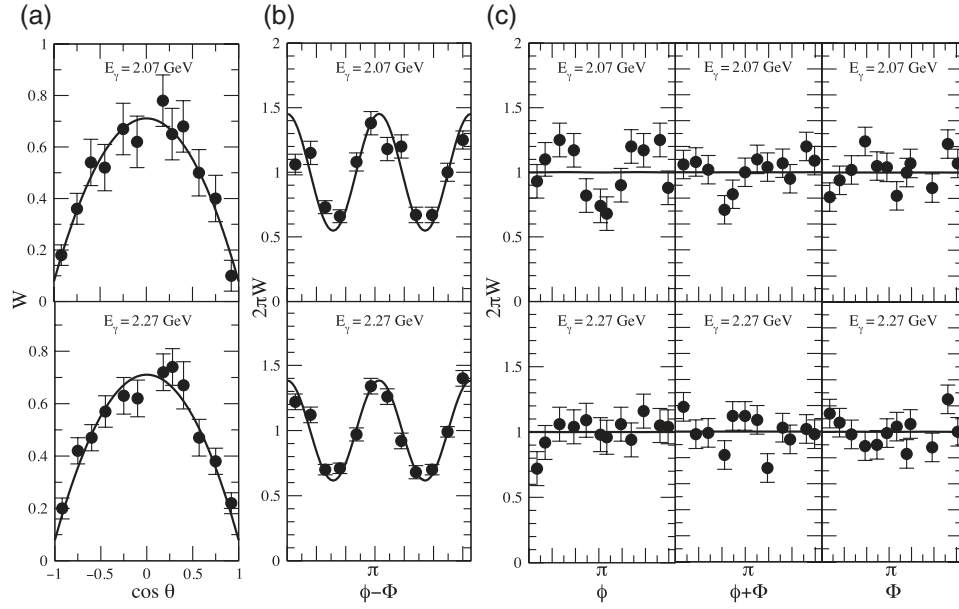
Fig. 11. The decay angular distributions for $-0.2 < t + |t|_{\min}$ in the Gottfried–Jackson frame. We take the center values of the energy ranges measured by the LEPS collaboration [4], i.e. $E_\gamma = 2.07\,\text{GeV}$ and $E_\gamma = 2.27\,\text{GeV}$. The experimental data are taken from Ref. [4].

local maximum, respectively. Therefore, we have computed the decay angular distributions at two photon energies, i.e. $E_\gamma = 2.07\,\text{GeV}$ and $E_\gamma = 2.27\,\text{GeV}$, which correspond to the center values of the given ranges of E_γ in the LEPS experiment.

The one-dimensional decay angular distributions $W(\cos\theta)$, $W(\phi - \Phi)$, $W(\phi)$ are presented in Fig. 11, and are expressed respectively as

$$W(\cos\theta) = \frac{1}{2}(1 - \rho^0_{00}) + \frac{1}{2}\left(3\rho^0_{00} - 1\right)\cos^2\theta,$$

$$2\pi W(\phi - \Phi) = 1 + 2p_\gamma \overline{\rho}^1_{1-1}\cos 2(\phi - \Phi),$$

$$2\pi W(\phi) = 1 - 2\text{Re}\,\rho^0_{1-1}\cos 2\phi,$$

$$2\pi W(\phi + \Phi) = 1 + 2p_\gamma \Delta_{1-1}\cos 2(\phi + \Phi),$$

$$2\pi W(\Phi) = 1 + 2p_\gamma \rho'\cos 2\Phi, \tag{18}$$

where θ and ϕ denote the polar and azimuthal angles of the decay particle K^+ in the GJ frame. Φ represents the azimuthal angle of the photon polarization in the center-of-mass frame. P_γ stands for the degree of polarization of the photon beam. $\overline{\rho}^1_{1-1}$, Δ_{1-1}, and ρ' are defined as

$$\overline{\rho}^1_{1-1} = \frac{1}{2}(\rho^1_{1-1} - \text{Im}\,\rho^2_{1-1}),$$

$$\Delta_{1-1} = \frac{1}{2}(\rho^1_{1-1} + \text{Im}\,\rho^2_{1-1}),$$

$$\rho' = 2\rho^1_{11} + \rho^1_{00}. \tag{19}$$

The expressions for the spin-density matrix elements $\rho^\alpha_{\lambda\lambda'}$ with the helicities λ and λ' for the ϕ meson can be found in Appendix A.

Panel (a) of Fig. 11 draws the one-dimensional decay polar-angle distributions $W(\cos\theta)$. As pointed out by Refs. [4,6], the decay distribution behaves approximately as $\sim (3/4)\sin^2\Psi$, which

Table 4. ϕ density matrix in the forward scattering at $E_\gamma = 2\,\mathrm{GeV}$

	ρ^0_{00}	$\overline{\rho}^1_{1-1}$	Re ρ^0_{1-1}	Δ_{1-1}	ρ'
t-channel $\pi^0 + \eta$	0	-0.5	0	0	0
ρN	0.651	-0.175	2.97×10^{-4}	-8.94×10^{-6}	1.37×10^{-2}
ωN	0.035	-0.48	9.26×10^{-4}	-8.72×10^{-7}	-1.05×10^{-3}
σN	0.254	-0.066	-8.85×10^{-3}	2.03×10^{-4}	-7.93×10^{-4}
πN	0.061	0.448	5.57×10^{-4}	1.79×10^{-4}	1.15×10^{-3}
$K\Lambda(1116)$	0.025	0.488	-1.08×10^{-2}	7.85×10^{-5}	-2.21×10^{-2}
$K^*\Lambda(1116)$	0.030	0.485	1.39×10^{-3}	1.10×10^{-6}	2.06×10^{-3}
$K^+\Lambda(1520)$	3.1×10^{-4}	0.499	-2.95×10^{-3}	5.131×10^{-6}	-6.02×10^{-3}
rescattering	6.62×10^{-2}	0.455	2.46×10^{-4}	1.74×10^{-4}	5.69×10^{-4}
hadrons	5.13×10^{-2}	0.24	5.64×10^{-4}	1.34×10^{-4}	-1.99×10^{-4}

indicates that the helicity-conserving processes are dominant as shown in Eq. (18). This means that t-exchange particles with unnatural parity at the tree level do not contribute to $W(\cos\theta)$. As will be discussed later, ρ^0_{00} from the π and η exchanges, which is related to the single spin-flip amplitude in the GJ frame, exactly vanishes. On the other hand, all hadronic rescattering diagrams contribute to it. Though the Pomeron exchange might contribute to this spin-density matrix element, it does not play any role below 2.3 GeV. Panel (b) of Fig. 11 shows the results of $W(\phi - \Phi)$, which are in good agreement with the LEPS data, whereas Panel (c) depicts those of $W(\phi)$, $W(\phi + \Phi)$, and $W(\Phi)$, respectively, which deviate from the data. In fact, the data show somewhat irregular behavior which does not seem to be easily reproduced.

As shown in Fig. 11, the decay angular distributions shed light on the production mechanism of the ϕ meson, since they make it possible to get access experimentally to the spin-density matrix elements, or the helicity amplitudes of ϕ photoproduction. It has important physical implications, because even though some diagrams seem to contribute negligibly to the cross sections, they might have definite effects on the decay angular distributions. In Table 4, the contributions of each rescattering diagram to the various spin-density matrix elements at $E_\gamma = 2\,\mathrm{GeV}$ are listed. As expected, the π and η exchanges contribute only to $\overline{\rho}^1_{1-1}$. The hadronic rescattering diagrams mainly contribute to ρ^0_{00} and $\overline{\rho}^1_{1-1}$, and are almost negligible to other components. Interestingly, the ρp rescattering diagram is the dominant one for ρ^0_{00}, even though it provides much smaller effects on the differential cross section than the $K\Lambda^*(1520)$ one.

Recently, the LEPS experiment measured the spin-density matrix elements for $\gamma p \to \phi p$ [6] in the range of $E_\gamma = 1.6$–$2.4\,\mathrm{GeV}$ in which the Pomeron exchange does not play a particularly important role in the present approach. Thus, we can examine the hadronic contributions to each spin-density matrix element. Figure 12 illustrates the various spin-density matrix elements, compared with the LEPS data. Since the experimental data are given in the finite range of E_γ, we just take the three center values corresponding to the ranges, i.e. $E_\gamma = 1.87, 2.07, 2.27\,\mathrm{GeV}$. The hadronic diagrams considered in the present work describe quantitatively Re ρ^0_{10}, ρ^0_{1-1}, and ρ^1_{11}. However, the deviations are found in other spin-density matrix elements as $t - |t|_{\min}$ increases.

4.   Summary and outlook

In the present work, we aimed at investigating the coupled-channel effects arising from the hadronic intermediate rescattering diagrams to ϕ photoproduction near the threshold region in addition to the conventional approach of Pomeron, π, and η exchanges. In particular, the bump-like structure
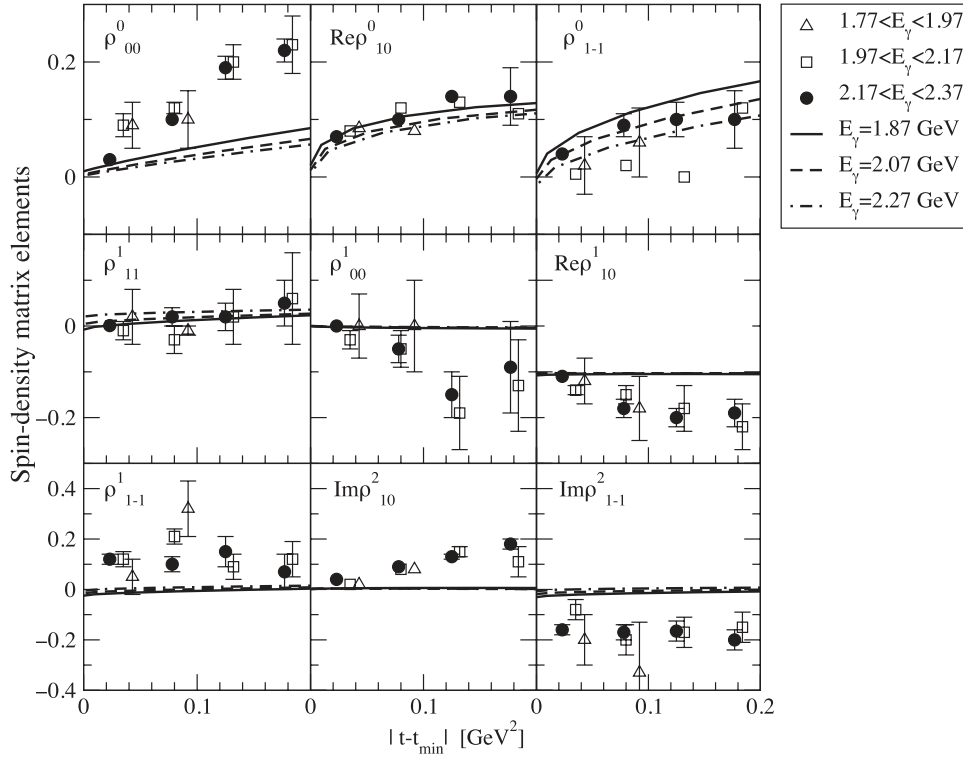
Fig. 12. The density matrix elements as a function of $|t - t_{\min}|$ for three different photon energies, i.e. 1.87 GeV, 2.07 GeV, and 2.27 GeV, to which the solid, dotted, and dot-solid curves correspond. The experimental data with three different ranges of the photon energy are taken from Ref. [6].

near $E_\gamma \approx 2.3$ GeV, which was reported by the LEPS experiment [4], sheds light on the production mechanism of the ϕ meson in the vicinity of the threshold, since the Pomeron exchange could not explain this peculiar structure of ϕ photoproduction. Thus, we studied in detail the effects of the seven different rescattering diagrams such as ρN, ωN, σN, πN, $K \Lambda(1116)$, $K^* \Lambda(1116)$, and $K \Lambda(1520)$ with the Pomeron exchange mechanism suppressed near the threshold region. In order to take into account the rescattering terms, we employed the Landau–Cutkosky rule in dealing with these rescattering diagrams.

Since it turned out that the $K \Lambda^*(1520)$ rescattering diagram played a dominant role among hadronic contributions in the lower-energy region, we scrutinized its contribution to ϕ photoproduction. We introduced form factors depending on both the s and t Mandelstam variables in such a way that the total cross section of the $\gamma p \to K \Lambda^*(1520)$ reaction was reproduced well. All other rescattering diagrams were constructed by utilizing the previous theoretical works and by reproducing the corresponding experimental data when they were available. We examined each contribution carefully by computing the differential cross section of ϕ photoproduction. While the $K \Lambda^*$ rescattering diagram was found to be the most dominant near 2 GeV, all other rescattering diagrams turned out to be very small. The results were in good agreement with the LEPS data, including the bumplike structure. We also computed the differential cross section as a function of $t + |t|_{\min}$ and found it to be in good agreement with the experimental data.

We investigated the contributions of hadronic rescattering diagrams to the decay angular distributions. While the one-dimensional angular distributions $W(\cos \theta)$ and $W(\phi - \Phi)$ were in good agreement with the experimental data, the other three angular distributions seemed to deviate from

the LEPS experimental data. We also examined the various spin-density matrix elements, which were measured recently by the LEPS collaboration. We found that the hadronic rescattering diagrams describe the experimental data for Re ρ_{10}^0, ρ_{1-1}^0, and ρ_{11}^1 well. While the present results explain near $t - |t|_{\min} \approx 0$ relatively well for other spin-density matrix elements, they deviated from the expeimental data as $t - |t|_{\min} \approx 0$ increased. Therefore, the conclusion of the present work is that the production mechanism of ϕ photoproduction near the threshold is governed by the hadronic coupled-channel effects, whereas the Pomeron only becomes important in the higher energy region.

As shown in the present work, the intermediate rescattering amplitudes, in particular the $K\Lambda^*(1520)$ one, play crucial roles in explaining the cross sections of the $\gamma p \to \phi p$ reaction in the vicinity of the threshold. Other rescattering diagrams also provided certain effects on the part of the spin-density matrix elements. We have considered in this work only the imaginary part of the transition amplitudes of the rescattering diagrams based on the Landau–Cutkosky rule. However, the results of the spin-density matrix elements already indicate that we should carry out a theoretical analysis of ϕ photoproduction more systematically and quantitatively. Thus, we need to investigate a full coupled-channel formalism and to solve rescattering equations (1) with the real parts of the rescattering diagrams fully taken into account. Another interesting and important problem is to extend our approach to the neutron target, since some of the considered amplitudes are isospin dependent. The corresponding works are under way.

Appendix A.   The spin-density matrix elements

The spin-density matrix elements are expressed in terms of the helicity amplitudes [5,48]:

$$\rho_{\lambda\lambda'}^0 = \frac{1}{N} \sum_{\lambda_\gamma, \lambda_i, \lambda_f} T_{\lambda_f, \lambda; \lambda_i, \lambda_\gamma} T_{\lambda_f, \lambda'; \lambda_i, \lambda_\gamma}^*,$$

$$\rho_{\lambda\lambda'}^1 = \frac{1}{N} \sum_{\lambda_\gamma, \lambda_i, \lambda_f} T_{\lambda_f, \lambda; \lambda_i, -\lambda_\gamma} T_{\lambda_f, \lambda'; \lambda_i, \lambda_\gamma}^*,$$

$$\rho_{\lambda\lambda'}^2 = \frac{i}{N} \sum_{\lambda_\gamma, \lambda_i, \lambda_f} \lambda_\gamma T_{\lambda_f, \lambda; \lambda_i, -\lambda_\gamma} T_{\lambda_f, \lambda'; \lambda_i, \lambda_\gamma}^*,$$

$$\rho_{\lambda\lambda'}^3 = \frac{1}{N} \sum_{\lambda_\gamma, \lambda_i, \lambda_f} \lambda_\gamma T_{\lambda_f, \lambda; \lambda_i, \lambda_\gamma} T_{\lambda_f, \lambda'; \lambda_i, \lambda_\gamma}^*, \tag{A1}$$

where λ_γ, λ_i, and λ_f represent the helicities for the photon and the initial and final nucleons, respectively, whereas λ and λ' denote those for the ϕ meson. The normalization factor N is defined as

$$N = \sum |T_{\lambda_f, \lambda; \lambda_i, \lambda_\gamma}|^2. \tag{A2}$$

References

[1] Z. Ahmed et al. [HAPPEX Collaboration], Phys. Rev. Lett. **108**, 102001 (2012) [arXiv:1107.0913 [nucl-ex]], and references therein.

[2] S. Donnachie, G. Dosch, P. Landshoff, and O. Nachtmann, *Pomeron Physics and QCD* (Cambridge University Press, Cambridge, UK, 2002), and references therein.

[3] F. E. Close and A. Donnachie, in *Electromagnetic Interactions and Hadronic Structure* eds. F. Close, S. Donnachie, and G. Shaw, (Cambridge University Press, Cambridge, UK, 2007).

[4] T. Mibe et al. [LEPS Collaboration], Phys. Rev. Lett. **95**, 182001 (2005) [arXiv:nucl-ex/0506015 [nucl-ex]].

[5] A. I. Titov, T.-S. H. Lee, H. Toki, and O. Streltsova, Phys. Rev. C **60**, 035205 (1999).

[6] W. C. Chang et al. [LEPS Collaboration], Phys. Rev. C **82**, 015205 (2010) [arXiv:1006.4197 [nucl-ex]].

[7] J. Beringer et al. [Particle Data Group], Phys. Rev. D **86**, 010001 (2012).

[8] S. Ozaki, A. Hosaka, H. Nagahiro, and O. Scholten, Phys. Rev. C **80**, 035201 (2009) [arXiv:0905.3028[hep-ph]]; **81**, 059901 (2010) [erratum].

[9] S.-I. Nam, A. Hosaka, and H.-Ch. Kim, Phys. Rev. D **71**, 114012 (2005) [arXiv:nucl-ex/0503149 [hep-ph]].

[10] A. Kiswandhi and S. N. Yang, Phys. Rev. C **86**, 015203 (2012) [arXiv:1112.6105 [nucl-th]]; **86**, 019904 (2012) [erratum].

[11] A. Kiswandhi, J.-J. Xie, and S. N. Yang, Phys. Lett. B **691**, 214 (2010) [arXiv:1005.2105 [hep-ph]].

[12] L. D. Landau, Nucl. Phys. **13**, 181 (1959).

[13] R. E. Cutkosky, J. Math. Phys. **1**, 429 (1960).

[14] R. Blankenbecler and R. Sugar, Phys. Rev. **142**, 1051 (1966).

[15] A. Donnachie and P. V. Landshoff, Phys. Lett. B **185**, 403 (1987).

[16] A. I. Titov and T. S. H. Lee, Phys. Rev. C **67**, 065205 (2003) [arXiv:nucl-ex/0305002 [nucl-th]].

[17] A. I. Titov and B. Kampfer, Phys. Rev. C **76**, 035202 (2007) [arXiv:0705.2010[nucl-th]].

[18] R. Machleidt, Adv. Nucl. Phys. **19**, 189 (1989).

[19] T. A. Rijken, Phys. Rev. C **73**, 044007 (2006) [arXiv:nucl-ex/0603041 [nucl-th]].

[20] A. I. Titov and T. S. H. Lee, Phys. Rev. C **66**, 015204 (2002).

[21] U.-G. Meissner, V. Mull, J. Speth, and J. W. van Orden, Phys. Lett. B **408**, 381 (1997) [arXiv:nucl-ex/9701296 [hep-ph]].

[22] P. Mergell, U. G. Meissner, and D. Drechsel, Nucl. Phys. A **596**, 367 (1996) [arXiv:nucl-ex/9506375 [hep-ph]].

[23] R. A. Adelseck, C. Bennhold, and L. E. Wright, Phys. Rev. C **32**, 1681 (1985).

[24] B. Friman and M. Soyeur, Nucl. Phys. A **600**, 477 (1996) [arXiv:nucl-ex/9601028 [nucl-th]].

[25] H. Kaneko, A. Hosaka, and O. Scholten, Eur. Phys. J. A **48**, 56 (2012) [arXiv:1112.4776 [hep-ph]].

[26] A. Kiswandhi and S. N. Yang, AIP Conf. Proc. **1432**, 323 (2012) [arXiv:1108.1657 [nucl-th]].

[27] K. H. Glander et al., Eur. Phys. J. A **19**, 251 (2004) [arXiv:nucl-ex/0308025 [nucl-ex]].

[28] R. Bradford et al. [CLAS Collaboration], Phys. Rev. C **73**, 035202 (2006).

[29] M. Sumihama et al. [LEPS Collaboration], Phys. Rev. C **73**, 035214 (2006) [arXiv:nucl-ex/0512053 [hep-ex]].

[30] K. Hicks et al. [LEPS Collaboration], Phys. Rev. C **76**, 042201 (2007).

[31] P. Achenbach et al., Eur. Phys. J. A **48**, 14 (2012) [arXiv:1104.4245 [nucl-ex]].

[32] K. Hicks, D. Keller and W. Tang, AIP Conf. Proc. **1374**, 177 (2011) [arXiv:1012.3129 [nucl-ex]].

[33] S. Janssen, J. Ryckebusch, W. Van Nespen, D. Debruyne, and T. Van Cauteren, Eur. Phys. J. A **11**, 105 (2001) [arXiv:nucl-ex/0105008 [nucl-th]].

[34] Y. Oh and H. Kim, Phys. Rev. C **73**, 065202 (2006) [arXiv:nucl-ex/0602112 [hep-ph]].

[35] Y. Oh and H. Kim, Phys. Rev. C **74**, 015208 (2006) [arXiv:nucl-ex/0605105 [hep-ph]].

[36] B. G. Yu, T. K. Choi, and W. Kim, Phys. Lett. B **701**, 332 (2011) [arXiv:1104.3672 [nucl-th]].

[37] S.-H. Kim, S.-i. Nam, Y. Oh, and H.-Ch. Kim, Phys. Rev. D **84**, 114023 (2011) [arXiv:1110.6515 [hep-ph]].

[38] K. Nakayama, Y. Oh, and H. Haberzettl, Phys. Rev. C **74**, 035205 (2006).

[39] A. I. Titov, H. Ejiri, H. Haberzettl, and K. Nakayama, Phys. Rev. C **71**, 035203 (2005) [arXiv:nucl-ex/0410098 [nucl-th]].

[40] A. I. Titov, B. Kämpfer, abd B. L. Reznik, Phys. Rev. C **65**, 065202 (2002).

[41] T. Sato and T.-S. H. Lee, Phys. Rev. C **54**, 2660 (1996).

[42] C. Wu et al., Eur. Phys. J. A **23**, 317 (2005).
[43] [Aachen–Berlin–Bonn–Hamburg–Hedielberg–Munich Collaboration], Phys. Rev. **175**, 1669 (1968).
[44] [Brown–Harvard–MIT–Padova–Weizmann Institute Bubble Chamber Group], Phys. Rev. **155**, 1468 (1967).
[45] H. J. Besch, G. Hartmann, R. Kose, F. Krautschneider, W. Paul, and U. Trinks, Nucl. Phys. **70**, 257 (1974).
[46] J. Ballam et al., Phys. Rev. D **7**, 3150 (1973).
[47] K. Gottfried and J. D. Jackson, Nuovo Cimento **33**, 309 (1964).
[48] K. Schilling, P. Seyboth, and G. E. Wolf, Nucl. Phys. B **15**, 397 (1970); **18**, 332 (1970) [erratum].
[49] J. Barth et al., Eur. Phys. J. A **17**, 269 (2003).